Nano Research

Open Access

Research Article

R2R fabrication of multiply indented, hybrid 3D-nanobowls with ultra-high haze for efficiently light trapping

Jingchen Zhang [1,§], Congming Li [1,2,§], Zhangjian Li [3], Zhebo Ren [1], Xiangming Li [1,2] ✉, Ye Tang [2,4,5], Guifang Liu [2], Xinkai Zhu [1], Yangfan Qiu [1], Hongmiao Tian [1], Liang Wang [2], and Jinyou Shao [1,2] ✉

[1] *Micro-/Nano-technology Research Center, State Key Laboratory for Manufacturing Systems Engineering, Xi'an Jiaotong University, Xi'an 710049, China*
[2] *Frontier Institute of Science and Technology, and Interdisciplinary Research Center of Frontier science and technology, Xi'an Jiaotong University, Xi'an 710049, China*
[3] *Future Technology Institute, Xi'an Jiaotong University, Xi'an 710049, China*
[4] *Beijing Institute of Remote Sensing Equipment, Beijing 100854, China*
[5] *Institute of Metallurgy and Environment, Central South University, Changsha 410083, China*
§ *Jingchen Zhang and Congming Li contributed equally to this work.*

Cite this article: *Nano Research*, **2026**, *19*, 94908395. https://doi.org/10.26599/NR.2026.94908395

ABSTRACT: Light trapping by nanostructures featuring high transmittance and high haze represents a viable strategy to boost solar cell efficiency via enhanced light absorption. However, low-cost, large-area, and eco-friendly fabrication approaches for such light trapping structures remain elusive. Herein, we demonstrate a new design of film with multiply indented, hybrid three-dimensional (3D)-nanobowls, which can reduce light reflection at large angles by together enhancing light scattering, transmittance, and haze. This kind of nanostructures is generated via roll-to-roll (R2R) UV-nanoimprint process, where the critical template is fabricated by taking advantage of metal displacement reaction between aluminum and zinc ions. The as-fabricated light-trapping film shows ultra-high haze of 98% while keeping favorable transmittance of 87%. Therefore, this light-trapping film, adhered onto polysilicon solar cells, enhances the short-circuit current (J_{SC}) from 4.26% at solar illumination angle of 0°, up to 65.95% at large angle of 85°, as well as 14.29% onto organic solar cells (OSC) under indoor light. To validate practical feasibility, day-time (13-hour) outdoor large-format polysilicon cells experiments reveal that the J_{SC} was enhanced by 5.68% under the sunny condition and 13.6% under the cloudy condition. Furthermore, this film exhibits self-cleaning performance with a water contact angle (WCA) of up to 140°. More importantly, this kind of high-performance film can be fabricated up to more than 25 m within 1 min using our R2R process, demonstrating the high throughput and low cost capability, well meeting the demand for solar cell industry.

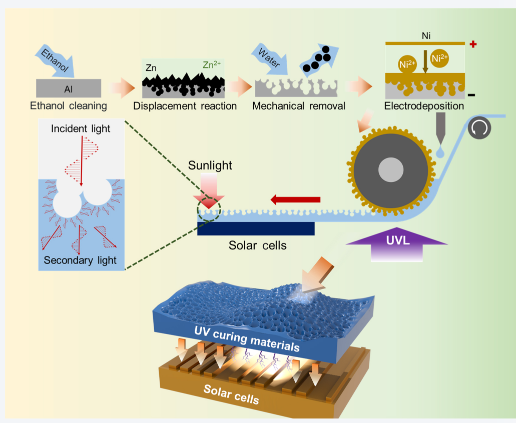

KEYWORDS: nanoimprinting, light trapping, transmittance, haze, solar cells

1 Introduction

As a renewable energy source that can be found everywhere, solar energy can provide people with inexhaustible energy to meet energy consumption needs. In the past few decades, great efforts have been devoted to the research of photovoltaic devices, such as silicon-based solar cells, organic solar cells (OSCs), dye-sensitized solar cells, and perovskite solar cells. How to reduce light reflection of solar cells and enhance light scattering inside them has increasingly become a research focus for improving the performance of solar cells. Traditional anti-reflective and light trapping microstructure fabricated on the silicon surface such as silicon nanowires (SiNW) [1–3], silicon pyramids [4–6], and silicon corrugation [7–9] have been confirmed that they can improve the photovoltaic conversion efficiency of solar cells. The current mainstream preparation methods are chemical etching, chemical growth, or laser grooving techniques. While highly effective, these methods inevitably damage the active layer and simultaneously introduce chemical instability, causing environmental pollution.

Received: October 28, 2025; **Revised:** December 30, 2025
Accepted: December 31, 2025

✉Address correspondence to Xiangming Li, xiangmingli@xjtu.edu.cn; Jinyou Shao, jyshao@xjtu.edu.cn

Anti-reflective (AR) coatings [10], designed to reduce light reflection and enhance transmittance via light interference cancellation, are fabricated through diverse techniques categorized into three main types: physical vapor deposition (PVD) [11, 12], chemical vapor deposition (CVD) [13, 14], and wet chemical methods [15–17]. Despite advancements, these techniques have inherent drawbacks: PVD and CVD demand expensive vacuum equipment; wet chemical films lack durability [18]. Most methods struggle with balancing uniformity on complex substrates, and some (e.g., CVD) pose environmental concerns, while large-scale production often faces trade-offs between cost, efficiency, and film performance.

With the advancement of micro/nanofabrication technologies, there has been a growing interest in light-trapping techniques for the front surfaces of solar cells. Front-surface light-trapping films, characterized by high haze, high transmittance, and low reflectance, enable effective light management at the external interface of solar cells, thereby avoiding damage to the internal active layers. Nanostructures such as nanospheres [19–21], nanocones [22, 23], nanopyramids [24–26], and nanobowls [27] can significantly increase the optical path length and reduce interfacial reflection, thereby playing a crucial role in enhancing the external quantum efficiency (EQE) and J_{SC} of solar cells.

Nanoimprinting, a microstructure fabrication technology with the advantage of high-throughput production, has not yet become the mainstream in front-surface light trapping mainly due to the difficulties in fabricating nanostructured metal templates: the fabrication of master templates primarily relies on silicon interface etching [28], making it difficult to achieve large-area R2R production [29]. Electroforming technology [30], as a processing method capable of large-area synchronous microstructure replication, can meet the demand for R2R nanoimprinting technology. Currently, the main metal microstructure generation technologies include electrochemical deposition [31–33], heat treatment [34, 35], chemical etching [36, 37], laser processing [38–40], etc. However, large-area microstructure generation-replication technologies that can fabricate nanostructures with consistent visible light wavelength scales (300–700 nm) in a large-area and environmentally friendly manner still remain to be developed.

To tackle the long-standing challenges in large-area light management for photovoltaic applications, we report the development of a scalable fabrication methodology for hybrid three-dimensional (3D)-nanobowls structures based on metal replacement reactions.Experimental studies demonstrate that submicron-scale morphological features generated via aluminum-zinc metal displacement reactions exhibit dimensional features matching the visible light spectrum. After removing zinc deposits from the aluminum substrate, a highly hybrid 3D-nanobowls topography is induced on the initially planar aluminum foil-evidenced by its macroscopic snow-white appearance, which indicates strong light scattering behavior. The polymer films embedded with this hierarchical structure exhibit remarkable optical properties, achieving an ultra-high haze of 98% and a transmittance of 87%, respectively. To enable R2R nanoimprinting, electroforming was employed for template fabrication, and a custom electroforming system was developed to produce large-format metal templates suitable for Al foil-based template replication. Integration of this large-format electroforming setup with R2R nanoimprinting equipment enabled continuous manufacturing of hybrid 3D-nanobowls polymer films. When attached to the front surface of solar cells, the hybrid 3D-nanobowls film drove substantial performance enhancements across diverse solar cell types, attributed to its superior light-trapping capability. Under 0°–85° solar illumination, polysilicon solar cells and OSCs exhibited J_{SC} enhancements of 4.26%–65.95% and 14.29% (indoor-light), respectively. These results underscore the negligible angular dependence and scalable fabrication capability of hybrid 3D-nanobowls, thus marking a significant breakthrough for front-surface light harvesting in large-area distributed photovoltaic systems.

2 Results and discussion

2.1 Hybrid 3D-nanobowls film preparation and characterization

Given the selection of R2R nanoimprinting as the scalable manufacturing approach, the fabrication of the hybrid 3D-nanobowls polymer films was systematically partitioned into two sequential modules: (i) microstructure generation and (ii) template replication. A schematic illustration of the complete process flow is presented in Fig. 1(a).

After ultrasonic cleaning of aluminum foil substrates in ethanol, a commercial zinc immersion solution was used for surface modification at a controlled temperature of 20 °C. Within 60 s of immersion, a densely packed layer of black zinc particles was observed to form spontaneously via displacement reaction. Scanning electron microscopy (SEM) analysis revealed the polyhedral morphology of these zinc particles, with dimensions ranging from 500 nm to 2.5 μm. Subsequently, rinsing with deionized water to remove the sacrificial zinc layer resulted in the formation of hybrid 3D-nanobowls with radius of 500–1000 nm on the aluminum substrate. The characteristic dimensions of these hierarchical structures, matching the visible light spectrum, imparted pronounced optical scattering effects. Macroscopically, the treated surface exhibited a uniform snow-white appearance, consistent with enhanced broadband Mie scattering at the subwavelength features.

Due to the insufficient hardness of aluminum substrates for direct use as nanoimprint templates, an electroforming process was developed to fabricate robust metallic templates. However, the high flexibility of aluminum foil means ordinary rack electroforming equipment fails to meet manufacturing requirements. To address this limitation, a custom-designed electroforming apparatus was engineered, featuring a metal cathode backplate-assisted configuration for ultrathin foil processing (Fig. S1(a) in the Electronic Supplementary Material (ESM)), with its schematic workflow shown in Fig. S1(b) in the ESM. The aluminum master was selectively etched using 25% NaOH solution, producing an 80 cm × 30 cm nickel template with 3D-nanospheres (Fig. 1(b)(i)). SEM confirmed the replicated structures retained hierarchical randomness, close-packing in the *x*–*y* plane, and distinct *z*-axis heterogeneity-morphological complexity expected to enhance broadband light scattering across the visible spectrum.

In early nanoimprinting trials, plate-to-plate processing caused frequent damage to polymer microstructures due to mechanical interlocking and anti-demolding forces (Fig. S2(c) in the ESM). Notably, transitioning to R2R nanoimprinting mitigated this issue significantly, as evidenced by reduced defect density in Figs. S2(a)

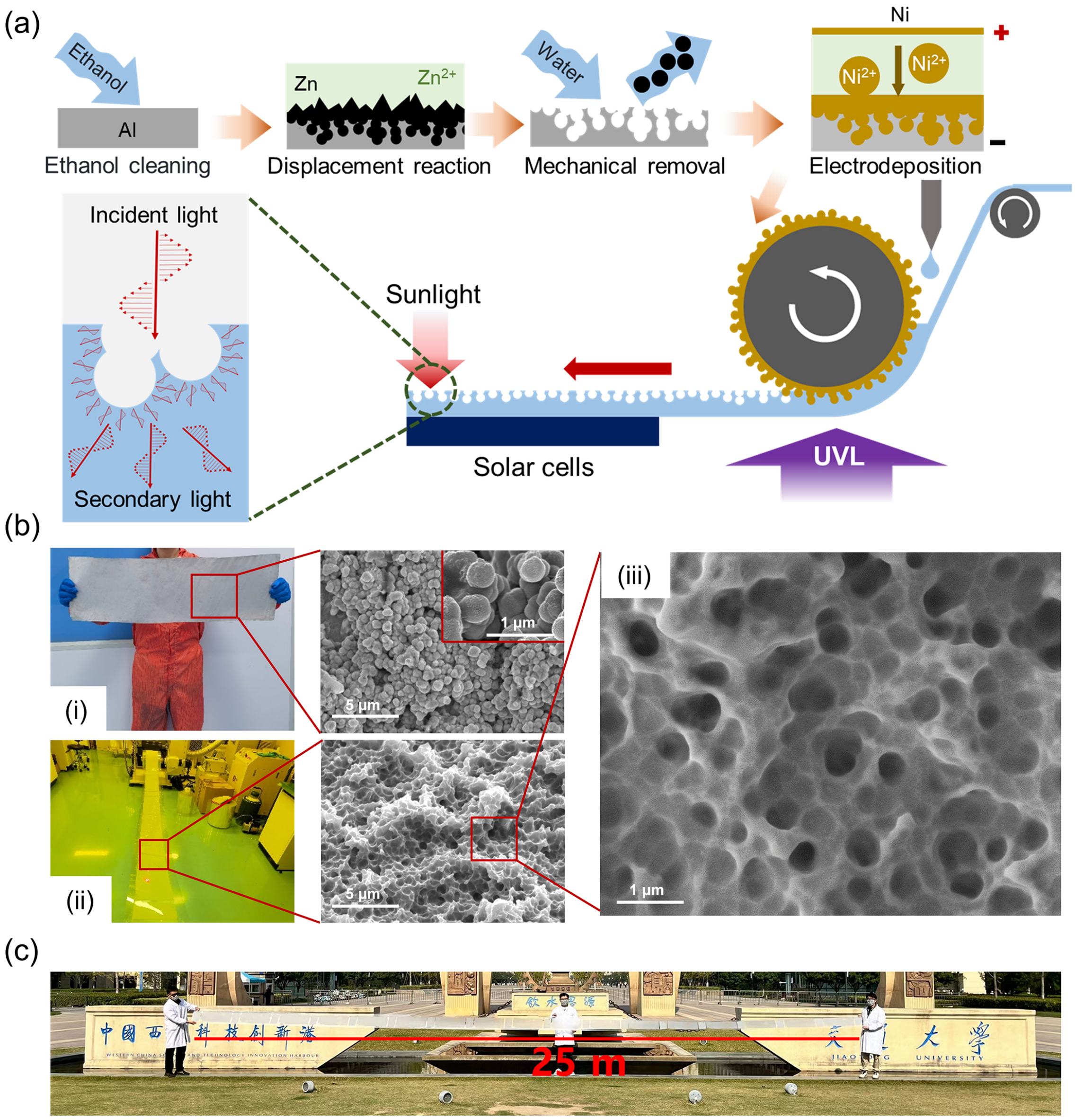

Figure 1 Preparation process, physical pictures and SEM images of hybrid 3D-nanobowls. (a) Schematic diagram of film preparation. (b) Physical pictures and SEM images: (i) metal template, (ii) R2R nanoimprinting process, and (iii) 3D-nanobowls. (c) Outdoor picture.

and S2(b) in the ESM. SEM analysis of the metal template and replicated polymer films at tilt angles of 0°, 20°, 40°, and 80° confirmed faithful replication of the *z*-axis topography, exhibiting characteristic wavy microstructures responsible for the observed high haze (Fig. S3 in the ESM). Leveraging the custom R2R nanoimprinting system, continuous production of large-area hybrid 3D-nanobowls films was achieved, as shown in the laboratory tests (Fig. 1(b)(ii) and 1(b)(iii)) and outdoor photographs (Fig. 1(c)). Figure S4 in the ESM offers a detailed view of the industrial-scale imprinting process, highlighting the scalability of this manufacturing approach.

2.2 Finite-difference time-domain (FDTD) optical simulation and experimental verification

To systematically characterize the optical properties of hybrid 3D-nanobowls and clarify their interaction mechanisms with incident light, FDTD simulations were conducted to model the electric field distribution within the films. Front-surface light management in photovoltaic devices encompasses two critical processes: (i) interface photon acceptance and (ii) internal light trapping.

In conventional planar solar cells, the abrupt refractive index mismatch at the air-polymer interface results in significant Fresnel reflection, leading to considerable light loss during photon acceptance and directly limiting device performance. Introducing nanobowls at the interface enables pronounced light-matter interactions: Owing to the matching of nanobowl diameters with visible light wavelengths, Mie scattering is triggered, manifesting as enhancement of light scattering. In this scenario, each nanobowl functions as an effective nano-concentrator, focusing incident sunlight onto the substructure region (Fig. 2(a)(i)).

However, the light-scattering effect of a single nanobowl structure remains limited. To expand the structure's scattering cross-section, we added an additional nanobowl along the *z*-axis. At this point, the light distribution inside the thin film is clearly more uniform (Fig. 2(a)(ii)), demonstrating that the hierachically stacked

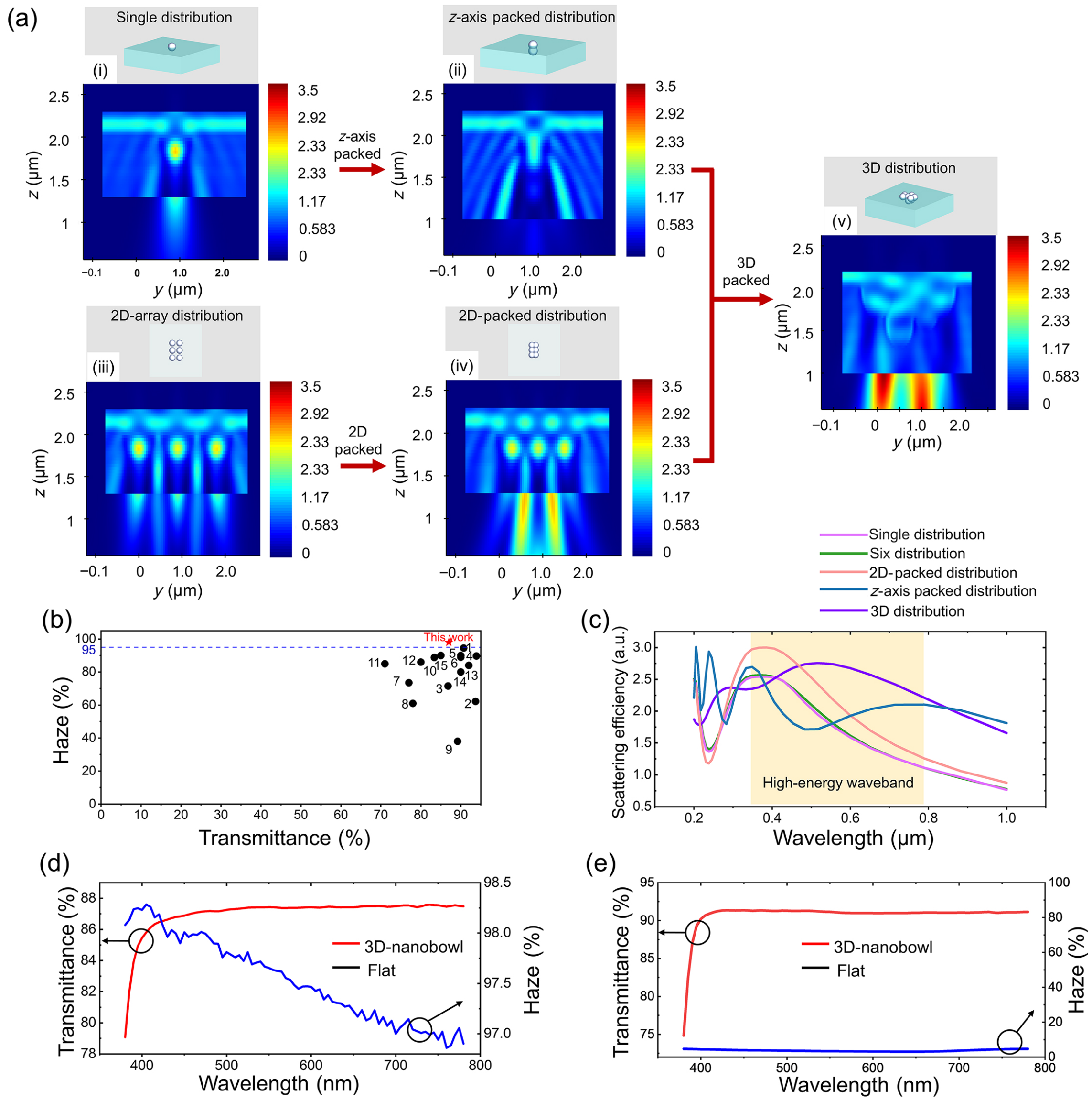

Figure 2 Optical simulation and experimental verification. (a) FDTD simulations of five different structural distributions: (i) single distribution, (ii) *z*-axis packed distribution, (iii) 2D-array distribution, (iv) 2D-packed distribution, and (v) 3D distribution. (b) Comparison of the performance between the present work and representative studies in recent years. (c) Scattering efficiencies of five different structures. (d) Optical properties of hybrid 3D-nanobowls films. (e) Optical properties of flat UV-curing films.

structure along the *z*-axis exerts a stronger light-scattering homogenization effect.

The distribution of nanobowls in the *x*–*y* plane also significantly impacts scattering efficiency. By comparing simulation results of two-dimensional (2D)-array and 2D-packed distributions (Figs. 2(a)(iii) and 2(a)(iv)), we found that nanobowls with 2D-array distribution exhibit a distinct light-concentrating effect, while their scattering efficiency matches that of a single nanobowl. This indicates that the scattering efficiency is not affected by the number of structures but only dependent on structural characteristics. Notably, when the structures are stacked in *x*–*y* plane, the stacked regions exhibit an enhanced scattering effect, resulting in higher scattering efficiency; here, the overlapping parts of nanobowls can be regarded as multiple nano-concentrators. This finding highlights that the highly close-packed stacking distribution of the nanobowl structure in the *x*–*y* plane will greatly facilitate the improvement of the film's scattering efficiency.

We further added a power monitoring analysis group to the original FDTD simulation model for backscattering ratio analysis. It can be seen from Fig. S5(a) in the ESM that within the spectral range of 200 to 1000 nm, the backscattering ratio of the nanobowl structures with *z*-axis stacked characteristics is significantly lower than that of the single nanobowl structures. This phenomenon is more pronounced in the *x*–*y* plane (Fig. S5(b) in the ESM). Due to the high similarity in the microstructural characteristics between close-packed and array-distributed nanobowls, their backscattering ratio trends exhibit a certain consistency. However, attributed to the secondary scattering effect of the overlapping regions, the close-packed nanobowl structures in the *x*–*y* plane show better suppression of backscattering ratio. Meanwhile, this is consistent with the scattering efficiency simulation results presented before.

By integrating the above-mentioned optimization strategies, we modeled the nanobowls that are highly randomly distributed both in the *z*-axis direction and *x*–*y* plane. As shown in Fig. 2(a)(v) in the ESM, as light passes through the hybrid 3D-nanobowls, it undergoes multiple scattering and is strongly concentrated directly beneath the structures. Analysis of the scattering cross-sections of structures with different distributions reveals that hybrid 3D-nanobowls exhibit the highest scattering efficiency in the high-energy band of sunlight (500–900 nm) show in Fig. 2(c) in the ESM.

To validate the simulated optical responses, optical characterization was performed. Ultraviolet–visible (UV–Vis) spectrophotometry was used to measure the transmittance and haze spectra of UV-curable flat films and hybrid 3D-nanobowls films (Figs. 2(d) and 2(e)). The flat polymer film exhibited a haze value of only 5% and a transmittance of 90%, approaching that of pure glass. In contrast, the hybrid 3D-nanobowls polymer film displayed exceptional optical scattering properties, attributed to its pronounced 3D structural heterogeneity. Its haze value exceeded 98% in the 400–500 nm spectral range, indicative of intensive multiple internal reflections that randomize light paths within the structured film. As the wavelength increased toward the far visible region, the haze gradually decreased to 97%, reflecting the reduced scattering efficiency of the nanostructures at longer wavelengths, which matches the results of FDTD simulation. Remarkably, despite the high haze (≥ 97%), the hybrid 3D-nanobowls film maintained a high average transmittance of 87% above 400 nm, a result of the synergistic light-concentrating effect of its hierarchical microstructure. As shown in Fig. 2(b) and Table S1 in the ESM, the optical performance of the film in this work ranks among the leading positions in studies on high-haze and high-transmittance optical films over the past ten years; in particular, its haze performance (98%) in the 400–500 nm spectral range far ahead in current research [41–55]. This dual characteristic of ultra-high haze and high transmittance demonstrates the film's superior performance in both interfacial light harvesting (via reduced specular reflection) and internal light trapping (via extended light lengths), representing an optimal balance for photovoltaic light management applications.

We employed a 532 nm laser pointer to conduct laser scattering experiments on the 3D-nanobowls films themselves. The planar UV-curable thin film has low haze, thus exhibiting almost no scattering effect on the laser. As can be clearly observed in Fig. S6(a) in the ESM, the incident point, reflection point, and transmission point of the laser are distinctly visible. In contrast, the film with 3D-nanobowls structures possesses ultra-high haze (98%), thereby demonstrating excellent light homogenization performance (Fig. S6(b) in the ESM).

2.3 Performance of different solar cells with 3D-nanobowls

Current research indicates that most 2D anti-reflective microstructures suffer from angular dependence, severely limiting their all-day outdoor applicability [56]. Thus, we conducted tests on the light trapping performance and photoelectric conversion performance of both polysilicon and OSCs under multi-angle incidence (0°, 30°, 60°, and 85°) and indoor light to verify the effectiveness of the 3D-nanobowls in practical application scenarios.

When a laser irradiates the surface of the planar polysilicon solar cell at a large angle, a significant amount of incident light is directly reflected (Fig. 3(a)). In contrast, the reflected light of the 3D-nanobowls-structured solar cells on their surfaces is notably reduced (Fig. 3(b)). This excellent light-trapping performance is attributed to the ultra-high haze and light-concentrating capability of the 3D-nanobowls films.

Subsequently, we conducted variable-angle photovoltaic conversion experiments on the two types of solar cells, and the schematic diagram is shown in Fig. 3(c). From Fig. 3(d), it can be observed that under large-angle illumination (60°), the surface-structured polysilicon solar cells exhibit a reduced reflectance across the entire visible wavelength range. Specifically, at 550 nm, the reflectance is only 17.7%, representing an 8.8% reduction compared to 19.4% for the planar polysilicon solar cells. This indicates that the surface-structured polysilicon solar cells can allow more light to enter the interior at the light-receiving interface. Observing the reflectance reduction at 550 nm (Fig. 3(g) and Fig. S7 in the ESM), it is evident that under multi-angle illumination, the 3D-nanobowls-structured solar cells consistently achieve a stable reduction in reflectance. This suggests that the antireflective performance of the 3D-nanobowls structures is insensitive to the incident angle of light.

As shown in Fig. 3(e), under large-angle illumination (60°), hybrid 3D-nanobowls induced a notable increase (33.02%) in J_{SC} for polysilicon cells, from 15.87 to 21.11 mA/cm^2, attributed to synergistic photonic concentrating and scattering effects. At other illumination angles (0°, 30°, 85°), the surface-structured polysilicon solar cells exhibit stable performance enhancement (Fig. 3(h) and Fig. S8 in the ESM). Meanwhile, we compared the integrated current of EQE with the results of *J*–*V* curves, and the two showed a highly consistent improvement ratio.

Due to the decrease in transmittance, the V_{OC} of the surface-structured solar cells exhibits a slight reduction. However, benefiting from the significant improvement in their J_{SC}, the peak power (P_{max}) of the surface-structured solar cells is remarkably superior to that of the surface-unstructured ones—under 60° solar irradiation conditions, P_{max} is increased by 26.31%. While both devices showed a decreasing trend in with increasing illumination angle, the magnitude of this decrease was far smaller for the surface-structured polysilicon solar cells-attributed to the excellent light trapping effect of the 3D-nanobowls. This result confirms that the 3D-nanobowls polysilicon solar cells can achieve considerable performance enhancement in practical application scenarios involving all-weather variations in solar illumination angles.

To further explain the enhancement in J_{SC} of polysilicon cells, we conducted EQE measurements. From Fig. 3(f), it is evident that under 60° illumination, the surface-structured polysilicon solar cells exhibited a substantial enhancement in EQE across the entire 400–1000 nm wavelength range. This result directly verifies that 3D-nanobowls enable the polysilicon solar cells to improve photoelectric conversion efficiency across the full high-energy wavelength spectrum under large-angle solar illumination-addressing the key challenge of efficiency degradation under off-normal incidence. Subsequent measurements at other illumination angles (0°, 30°, 85°) further confirmed that this EQE enhancement remained significant, demonstrating the structure's robust performance adaptability to diverse solar incidence conditions (Fig. 3(i) and Fig. S8 in the ESM).

To verify the versatility of this hybrid 3D-nanobowls across non-silicon-based solar cells， we further integrated it on the front surface of OSCs for comprehensive characterization. Distinct from silicon-based cells, OSCs are commonly deployed for indoor low-light energy harvesting, eliminating the need for multi-angle optical measurements. Figure 4(a) illustrates the light-trapping diagram and laser pen shooting picture: in planar configurations,

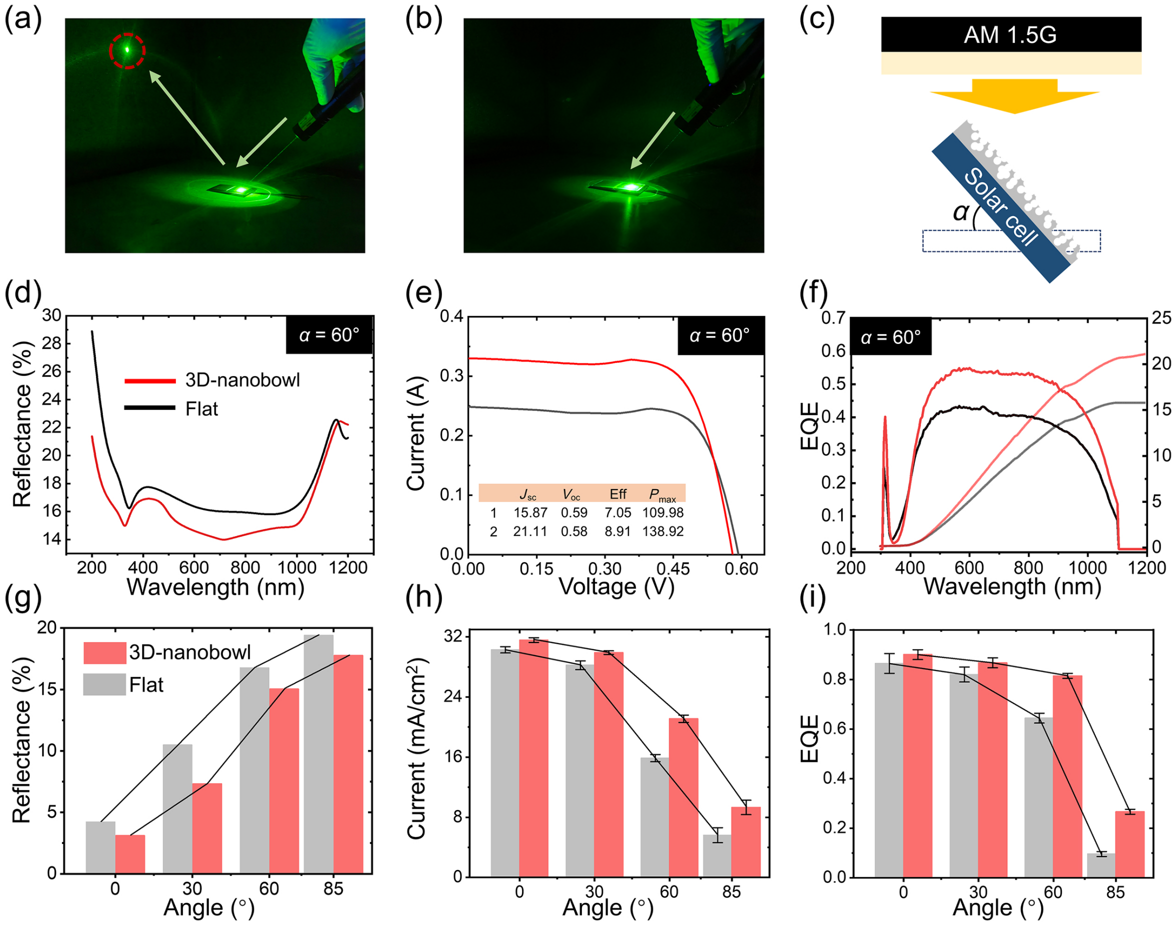

Figure 3 Performance of polysilicon solar cells. (a) Laser-irradiated planar cell. (b) Laser-irradiated structured cell. (c) Multi-angle solar spectrum irradiation test schematic diagram. (d) Reflectivity, (e) I–V curve (unit: J_{SC} (mA/cm²), V_{OC} (V), Eff (%), and P_{max} (mW)), and (f) EQE & integrated current curve under 60° irradiation. (g) Reflectivity, (h) J_{SC}, and (i) EQE (at 550 nm) under different irradiation angles (0°, 30°, 60°, 85°).

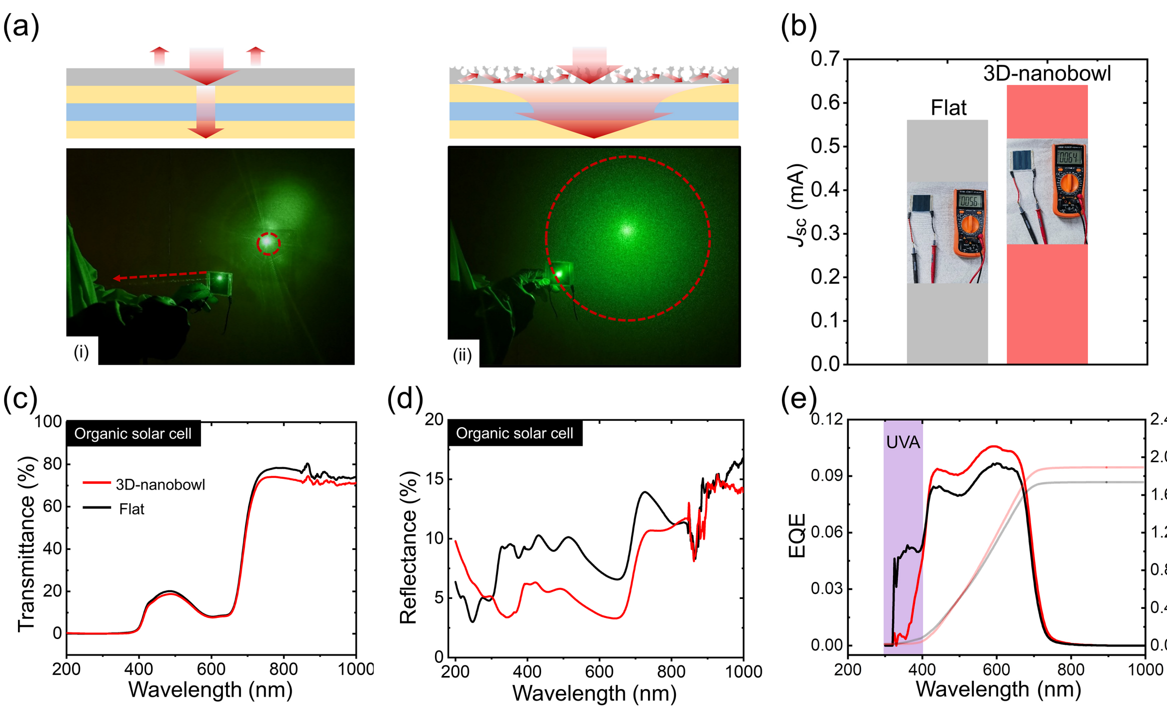

Figure 4 Testing of OSCs. (a) Light trapping diagram and laser pen shooting picture: (i) flat OSCs and (ii) 3D-nanobowls structured OSCs. (b) J_{SC} under indoor-light. (c) Transmittance properties. (d) Reflectivity properties. (e) EQE test.

considerable incident light is lost to specular reflection, whereas the hybrid 3D-nanobowls function as a dual-purpose diffuser and antireflective layer, reducing reflectance. It can also be observed that irradiation of planar OSCs produced a distinct specular reflection path and a compact transmitted spot, indicative of poor light diffusion. In contrast, the hybrid 3D-nanobowls structured OSC exhibited negligible specular reflection and a significantly expanded transmitted spot, directly demonstrating the nanostructure's enhanced light-scattering and antireflective capabilities.

Distinct from Si-based solar cells, OSCs require balanced transparency for tandem applications. As shown in Fig. 4(c), the hybrid 3D-nanobowls film induced only a marginal transmittance decrease in the near-infrared region (> 750 nm), while maintaining nearly unaltered transmittance in the visible spectrum. This demonstrates that the nanostructure does not compromise the optical transparency critical for organic device operation. Concurrently, reflectivity dropped to 5%, representing a 100% reduction relative to the initial 10% across the visible range (Fig. 4(d)), further validating the universal efficacy of the hybrid 3D-nanobowls in enhancing light utilization efficiency across diverse photovoltaic technologies.

EQE measurements revealed a pronounced reduction in the 300–360 nm UV band for structured OSCs, with EQE dropping below 0.5%—an order of magnitude lower than planar devices (Fig. 4(e)). This UV-shielding behavior underscores the universal applicability of the hybrid 3D-nanobowls in mitigating photo-induced degradation. Mechanistically, the nanostructure suppresses UV-induced polymer backbone cleavage and interface defect formation, thereby extending operational lifespan—a critical attribute for organic photovoltaic technologies [57]. In the high-energy spectral waveband spanning 440–640 nm, the structured OSCs exhibited a 1% absolute increase in EQE, corresponding to a relative percentage enhancement exceeding 10%. Under 16 W indoor daylight illumination, the structured OSCs achieved a J_{SC} of 0.64 mA, representing a 14.29% enhancement relative to planar controls (Fig. 4(b)). Collectively, these findings validate the suitability of the hybrid 3D-nanobowls for front-surface light trapping in organic photovoltaic devices, demonstrating its universal applicability across diverse solar cell technologies.

2.4 Outdoor and weather resistance performance verification

To address the performance degradation in outdoor distributed photovoltaic systems caused by dust accumulation and contamination, we investigated the self-cleaning properties of hybrid 3D-nanobowls. Current mainstream photovoltaic encapsulates (glass/resin) exhibit hydrophilic surfaces, leading to persistent dust adhesion that significantly reduces optical transmittance. The hybrid 3D-nanobowls, featuring a densely packed and randomly distributed nanoporous surface, provides a hierarchical topography conducive to super hydrophobic behavior, as characterized in Fig. 5(a). Mechanistically, raindrops impacting the solar cell surface acquire kinetic energy that facilitates dust removal. Upon contact with the hybrid 3D-nanobowls, liquid droplets form a Cassie-Baxter state, where air pockets trapped within the nanostructures support the droplet, resulting in a contact angle of 140°-notably higher than the 70° contact angle of resin-sealed planar surfaces (Fig. 5(b)). To quantify this self-cleaning behavior, we performed dust-removing experiments (Fig. 5(c)): Dust particles were uniformly deposited on the 3D-nanobowls film, and syringe-generated droplets (mimicking raindrops with impact kinetic energy) were applied. Observations showed that droplets rapidly rolled off the surface, with the resulting flow efficiently washing dust onto a collection cloth. This demonstrates that the hybrid 3D-nanobowls film enables rain-driven self-cleaning via its super hydrophobic topography, which minimizes liquid-solid contact area and maximizes roll-off efficiency.

To further validate the outdoor practical performance of hybrid 3D-nanobowls, large-format polysilicon solar cells were chosen for outdoor all-day characterization. Using UV-curable adhesives as an intermediate layer, R2R imprinted hybrid 3D-nanobowls films were laminated onto the cell surfaces, and experiments were conducted on a rooftop test platform. Figure 5(d) illustrates the all-day light management principle, where the 3D-nanobowls dynamically homogenize and concentrate sunlight across diurnal irradiation angles while reducing interfacial reflection losses. A representative photograph of the experimental setup is shown in Fig. 5(e). Figure 5(f) documents J_{SC} profiles of structured and planar polysilicon cells from 6 a.m. to 7 p.m. under respective sunny and cloudy conditions. Under clear-sky illumination (Figs. 5(f) and 5(i)), the structured cells consistently exhibited higher J_{SC} values. Although transient cloud cover caused fluctuations, the time-integrated short-circuit charge of the 3D-nanobowls-integrated solar cells reached 35.88 Ah, representing a 5.68% enhancement (1.93 Ah increase) over planar controls. This improvement stems from the 3D-nanobowls' angle-insensitive light trapping, which mitigates the diurnal decrease in effective illumination area. Under the cloudy condition (Fig. 5(f)(ii)), the J_{SC} exhibited greater stochasticity due to random variations in solar intensity and diffuse light distribution. Notably, surface-structured solar cells exhibited a 13.6% enhancement in time-integrated charge (from 26.19 to 29.75 Ah), with a more significant performance advantage over control devices than that under direct sunlight. This phenomenon is attributed to the superior diffuse light management capability of the hybrid 3D-nanobowls structure, which converts omnidirectional incident photons into extended optical paths within the active layer-a critical advantage for low-intensity, diffuse illumination scenarios. These findings highlight the dual functionality of hybrid 3D-nanobowls in enhancing both light trapping and surface self-cleaning, effectively addressing critical challenges in practical outdoor photovoltaic deployments.

3 Experimental

3.1 Electrodeposition parameters and power supply

To improve the quality of nickel metal templates, a custom dual-pulse power supply (ZXT-MC-200) was selected, with a maximum operating voltage of 15V and a maximum operating current of 200A. The electroplating parameter settings tested are shown in Table 1. The electroplating solution adopts a commercial nickel sulfa mate solution. The deposited metal layer exhibits high resilience and mechanical properties, meeting the application requirements of nano-imprinting metal templates.

3.2 FDTD simulation model settings

To study the characteristics of electric field distribution, we used FDTD simulation software to simulate hybrid 3D-nanobowls structure. On a UV-cured material with a thickness of 50 micrometers and a refractive index of 1.525, a porous structure

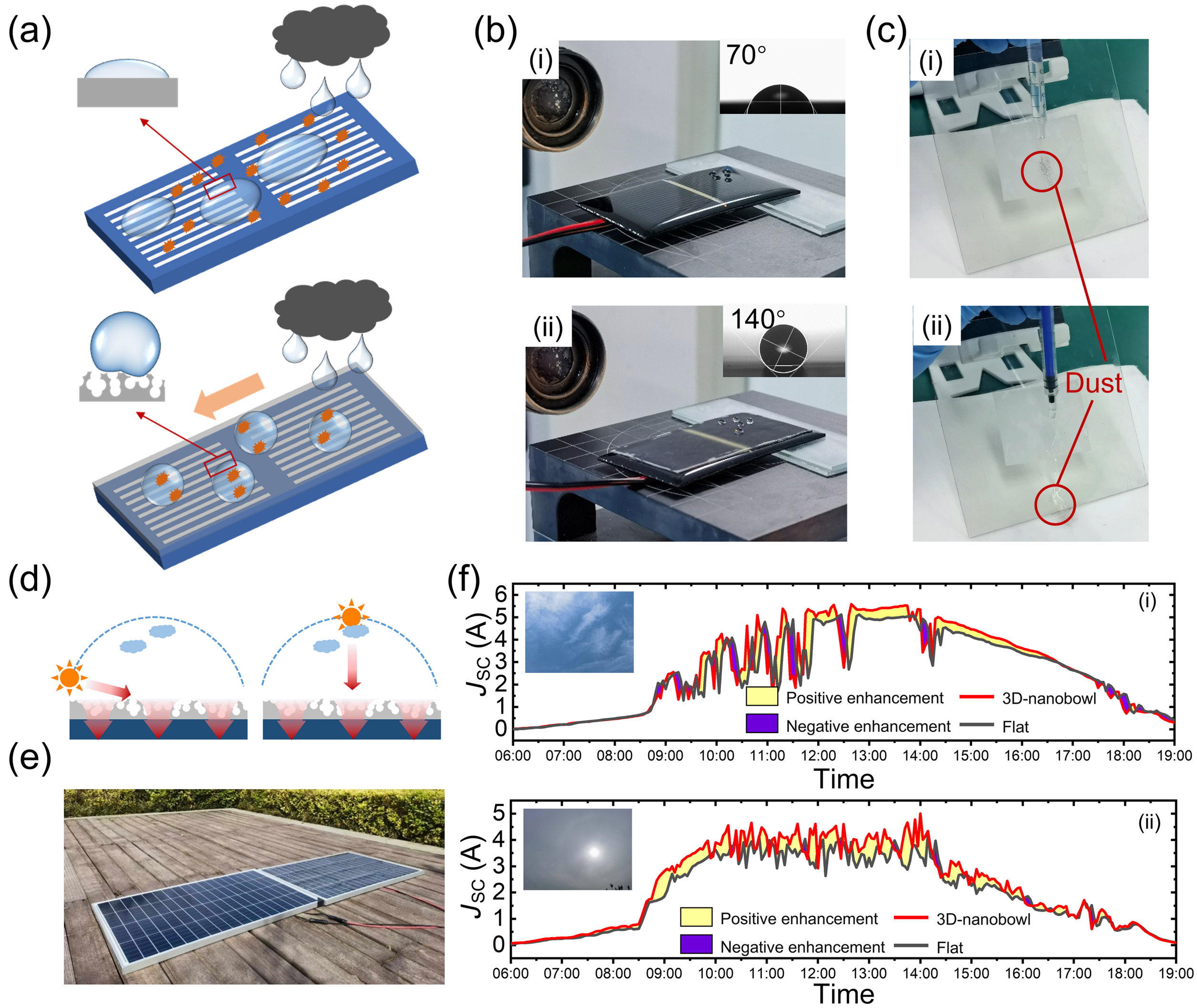

Figure 5 Surface self-cleaning performance and outdoor 13-h experiments. (a) Rainy day self-cleaning diagram. (b) Contact angle measurement: (i) flat polysilicon solar cell and (ii) 3D-nanobowls structured solar cell. (c) Dust-removing experiment: (i) before dust removal and (ii) after dust removal. (d) Schematic diagram of all-day sunlight capture. (e) Large-format polysilicon solar cell outdoor test actual picture. (f) All-day J_{sc} experiment (13 h) under different weather conditions: (i) sunny and (ii) cloudy.

Table 1 Electrodeposition parameters

Pulse output	Average current (A/m²)	Duty ratio	Working frequency (Hz)
Positive electrode	200	80%	2000
Negative electrode	75	50%	2500

was created using a Boolean operation to subtract a sphere with a diameter of 700 nm. A nonlinear Total-field scattered-field (TFSF) light source with a wavelength range of 200 to 1000 nm was selected to simulate sunlight. Scattering analysis groups and electric field monitors were set up around the structure to obtain the electric field distribution data of the structural films.

3.3 Contact angle and self-cleaning characterization

We utilized a contact angle meter (OCA-5OEC) to measure the contact angles of samples. The samples were prepared by attaching a hybrid 3D-nanobowls film to the surface of a polysilicon solar cell. Some dosing volume of 3 μL water droplets were dispensed onto the sample. Images were captured to document the contact angle measurements.

3.4 Optical characterization

We used a UV–VIS–NIR spectrophotometer (PE Lambda950) to test the reflectance of surface-structured solar cells in the wavelength range of 200 to 1000 nm, and conducted transmittance, reflectance, and haze tests on hybrid 3D-nanobowls films over a broad wavelength range of 200 to 2000 nm. The instrument was equipped with an integrated sphere with a highly reflective inner surface to collect both diffused and direct light.

3.5 Nanostructure characterization

Since the hybrid 3D-nanobowls are submicron in size, an electron microscope is required to characterize their specific morphology. We chose electron microscope (GeminiSEM-500) for the characterization of the nanostructures.

3.6 Performance characterization of solar cells

EQE measurements of three types of solar cells were conducted using a quantum efficiency measurement system across the 300–1000 nm wavelength range, with a circular illumination spot of 1 cm in diameter. The solar simulator (Newport Oriel) employs a 450 W xenon arc lamp as the light source, equipped with an AM 1.5G filter system for *J*–*V* curve measurements to obtain device performance parameters, including V_{OC}, J_{SC}, fill factor (FF), and power conversion efficiency (PCE). EQE measurement system (1000ADX, USA) characterizes the ratio of charge carriers to incident photons on the cell surface, reflecting the photovoltaic response of solar cells to different wavelength spectra.

4 Conclusions

Facing the cross-scale manufacturing challenges for front-surface nanostructured light-trapping in large-area distributed photovoltaic systems, we report an innovative microstructure fabrication strategy based on metal displacement reactions. This approach enables low-cost production of hybrid 3D-nanobowls metal templates (80 cm × 30 cm) and R2R imprinting of large-format hybrid 3D-nanobowls films, which exhibit exceptional optical properties: ultra-high haze of 98% and transmittance of 87%. Experimental characterizations demonstrate significant performance enhancements across diverse solar cell technologies. Under all-day field conditions, commercial large-format polysilicon cells achieve 5.68% and 13.6% increases in integrated short-circuit charge under sunny and cloudy conditions, respectively. The hierarchical nanoporous surface morphology endows the films with a super hydrophobic contact angle of 140°, enabling rain-driven self-cleaning to mitigate dust accumulation. Collectively, this work presents a versatile, cost-effective, and scalable front-surface light management strategy. The hybrid 3D-nanobowls integrate synergistic light-trapping and self-cleaning functionalities, showcasing substantial commercialization potential for next-generation distributed photovoltaic systems.

Electronic Supplementary Material: Supplementary material is available in the online version of this article at https://doi.org/10.26599/NR.2026.94908395.

Data availability

All data needed to support the conclusions in the paper are presented in the manuscript and the Electronic Supplementary Material. Additional data related to this paper may be requested from the corresponding author upon request.

Acknowledgements

The authors appreciate funding support from the National Natural Science Foundation of China (Nos. 52025065, 52322513, and 52350349) and the Shaanxi Provincial Key Project (Special Support) (No. 2023JC–XJ–15).

Declaration of competing interest

All the contributing authors report no conflict of interests in this work.

Author contribution statement

J. C. Z. was responsible for experimental design, experimental validation, writing the original draft of the paper, and data processing. C. M. L. was responsible for experimental validation and paper revision. Z. J. L. was responsible for experimental design and paper revision. Z. B. R. was responsible for data processing and experimental validation. X. M. L. and J. Y. S. were responsible for project management, paper review, and funding acquisition. Y. T. was responsible for experimental validation and experimental review. G. F. L., X. K. Z., Y. F. Q., H. M. T., and L. W. were responsible for paper revision.

Use of AI statement

During the preparation of this manuscript, the main body of the paper's cover was created using 3ds Max software, while the background rendering was generated with the Al tool: the Nano Banana module within Gemini. After using this tool, the author has reviewed and edited the relevant content as needed, and assumes full and exclusive responsibility for the content of this publication.

References

[1] Yu, P.; Wu, J.; Liu, S. T.; Xiong, J.; Jagadish, C.; Wang, Z. M. Design and fabrication of silicon nanowires towards efficient solar cells. *Nano Today* **2016**, *11*, 704–737.

[2] Chen, J. Y.; Subramani, T.; Sun, Y. L.; Jevasuwan, W.; Fukata, N. Efficiency enhancement of silicon nanowire solar cells by using UV/ozone treatments and micro-grid electrodes. *Appl. Surf. Sci.* **2018**, *439*, 1057–1064.

[3] Maity, D.; Pathak, S. K.; Deepa, M. Easy-to-fabricate high efficiency silicon nanowires solar cell modified by CdTe and zinc tetraphenyl porphyrin nanostructures. *J. Energy Chem.* **2021**, *63*, 484–497.

[4] Jiang, Y.; Shen, H. L.; Pu, T.; Zheng, C. F.; Tang, Q. T.; Gao, K.; Wu, J.; Rui, C. B.; Li, Y. F.; Liu, Y. W. High efficiency multi-crystalline silicon solar cell with inverted pyramid nanostructure. *Sol. Energy* **2017**, *142*, 91–96.

[5] Sun, Z. H.; Chen, W.; Zhang, X. H.; Xu, M.; Xing, G. G.; Chen, X. Q.; Feng, B. W.; Li, H. Z.; Ma, J. H.; Wang, Y. et al. Chain pyramid texturization for better light trapping and efficiency of silicon solar cells. *Sol. Energy Mater. Sol. Cells* **2023**, *251*, 112137.

[6] Chu, F. H.; Qu, X. L.; He, Y. C.; Li, W. L.; Chen, X. Q.; Zheng, Z. L.; Yang, M.; Ru, X. N.; Peng, F. G.; Qu, M. H. et al. Prediction of sub-pyramid texturing as the next step towards high efficiency silicon heterojunction solar cells. *Nat. Commun.* **2023**, *14*, 3596.

[7] Bahabry, R. R.; Kutbee, A. T.; Khan, S. M.; Sepulveda, A. C.; Wicaksono, I.; Nour, M.; Wehbe, N.; Almislem, A. S.; Ghoneim, M. T.; Sevilla, G. A. T. et al. Solar cells: Corrugation architecture enabled ultraflexible wafer-scale high-efficiency monocrystalline silicon solar cell. *Adv. Energy Mater.* **2018**, *8*, 1870055.

[8] Luo, Y.; Liu, S. Y.; Barange, N.; Wang, L.; So, F. Perovskite solar cells: Perovskite solar cells on corrugated substrates with enhanced efficiency. *Small* **2016**, *12*, 6345.

[9] El-Atab, N.; Babatain, W.; Bahabry, R.; Alshanbari, R.; Shamsuddin, R.; Hussain, M. M. Ultraflexible corrugated monocrystalline silicon solar cells with high efficiency (19%), improved thermal performance, and reliability using low-cost laser patterning. *ACS Appl. Mater. Interfaces* **2020**, *12*, 2269–2275.

[10] Adak, D.; Bhattacharyya, R.; Barshilia, H. C. A state-of-the-art review on the multifunctional self-cleaning nanostructured coatings for PV panels, CSP mirrors and related solar devices. *Renew. Sustain. Energy Rev.* **2022**, *159*, 112145.

[11] Momeni, S.; Tillmann, W.; Pohl, M. Composite cavitation resistant PVD coatings based on NiTi thin films. *Mater. Des.* **2016**, *110*, 830–838.

[12] Khan, S. B.; Irfan, S.; Zhang, Z. J. Fabrication and characterization of MgF_2 anti-reflective films comprising dual-layer prepared by physical vapor deposition technique for optoelectronic applications. *J. Mater. Res.Technol.* **2024**, *31*, 1616–1625.
[13] Vijselaar, W.; Elbersen, R.; Tiggelaar, R. M.; Gardeniers, H.; Huskens, J. Photo-electrical characterization of silicon micropillar arrays with radial p/n junctions containing passivation and anti-reflection coatings. *Adv. Energy Mater.* **2017**, *7*, 1601497.
[14] Shi, T.; Jia, Q.; Wang, H. N.; Chen, R. Y. Preparation of superhydrophobic and oleophobic antireflective coating with high transmittance. *Surf. Coati. Technol.* **2021**, *428*, 127863.
[15] Purcar, V.; Rădiţoiu, V.; Dumitru, A.; Nicolae, C. A.; Frone, A. N.; Anastasescu, M.; Rădiţoiu, A.; Raduly, M. F.; Gabor, R. A.; Căprărescu, S. Antireflective coating based on TiO_2 nanoparticles modified with coupling agents via acid-catalyzed sol–gel method. *Appl. Surf. Sci.* **2019**, *487*, 819–824.
[16] Lin, H. F.; Qiu, Z. Y.; Huang, P. N.; Zeng, L. L.; Liang, Y. F.; Zeng, C. H.; Lin, R. X.; Yuan, M. Y.; Hong, R. J. Preparation of antireflective coatings with moisture resistance and a widely tunable refractive index by combining the sol-gel method with evaporation concentration. *Constr. Build. Mater.* **2022**, *318*, 125810.
[17] Womack, G.; Isbilir, K.; Lisco, F.; Durand, G.; Taylor, A.; Walls, J. M. The performance and durability of single-layer sol–gel anti-reflection coatings applied to solar module cover glass. *Surf. Coati. Technol.* **2019**, *358*, 76–83.
[18] Sarkın, A. S.; Ekren, N.; Sağlam, Ş. A review of anti-reflection and self-cleaning coatings on photovoltaic panels. *Sol. Energy* **2020**, *199*, 63–73.
[19] Winkless, L. Nanospheres for omnidirectional solar cells. *Mater. Today* **2014**, *17*, 260.
[20] Luo, Q.; Deng, X. S.; Zhang, C. X.; Yu, M. D.; Zhou, X.; Wang, Z. B.; Chen, X. H.; Huang, S. M. Enhancing photovoltaic performance of perovskite solar cells with silica nanosphere antireflection coatings. *Sol. Energy* **2018**, *169*, 128–135.
[21] Esmaeilzad, N. S.; Demir, A. K.; Hajivandi, J.; Ciftpinar, H.; Turan, R.; Kurt, H.; Bek, A. Nanosphere concentrated photovoltaics with shape control. *Adv. Opt. Mater.* **2021**, *9*, 2000943.
[22] Jacobo-Martín, A.; Hernández, J. J.; Solano, E.; Monclús, M. A.; Martínez, J. C.; Fernandes, D. F.; Pedraz, P.; Molina-Aldareguia, J. M.; Kubart, T.; Rodríguez, I. Resilient moth-eye nanoimprinted antireflective and self-cleaning TiO_2 sputter-coated PMMA films. *Appl. Surf. Sci.* **2022**, *585*, 152653.
[23] Wang, S. X.; Cui, H.; Jin, S. J.; Pi, X. D.; He, H. Y.; Shou, C. H.; Yang, D. R.; Wang, L. Anti-reflection effect of high refractive index polyurethane with different light trapping structures on solar cells. *Heliyon* **2023**, *9*, e20264.
[24] Amalathas, A. P.; Alkaisi, M. M. Efficient light trapping nanopyramid structures for solar cells patterned using UV nanoimprint lithography. *Mater. Sci. Semicond. Proc.* **2017**, *57*, 54–58.
[25] Liu, D. M.; Wang, Q. K.; Wang, Q. Transfer the multiscale texture of crystalline Si onto thin-film micromorph cell by UV nanoimprint for light trapping. *Appl. Surf. Sci.* **2018**, *439*, 168–175.
[26] He, J. X.; Zheng, Q.; Ren, Z. Y.; Yu, J. L.; Deng, H.; Lai, Y. F.; Cheng, S. Y. 10.18% PCE of organic solar cells with pyramid micron-structured PDMS. *Solar Energy* **2021**, *220*, 394–399.
[27] Zhang, M.; Deng, Q. L.; Shi, L. F.; Cao, A. X.; Pang, H.; Hu, S. Nanobowl array fabrication based on nanoimprint lithography. *Optik* **2016**, *127*, 145–147.
[28] Chen, J. Y.; Sun, K. W. Enhancement of the light conversion efficiency of silicon solar cells by using nanoimprint anti-reflection layer. *Sol. Energy Mater. Sol. Cells* **2010**, *94*, 629–633.
[29] Ahn, S. H.; Guo, L. J. Large-area roll-to-roll and roll-to-plate nanoimprint lithography: A step toward high-throughput application of continuous nanoimprinting. *ACS Nano* **2009**, *3*, 2304–2310.
[30] Zhang, H. G.; Zhang, N.; Gilchrist, M.; Fang, F. Z. Advances in precision micro/nano-electroforming: A state-of-the-art review. *J. Micromech. Microeng.* **2020**, *30*, 103002.
[31] Dos Santos Claro, P. C.; Castez, M. F.; Schilardi, P. L.; Luque, N. B.; Leiva, E. P. M.; Salvarezza, R. C. Spontaneous nanoripple formation on metallic templates. *ACS Nano* **2008**, *2*, 2531–2539.
[32] Pratama, K.; Tian, C. H.; Schürch, P.; Casari, D.; Watroba, M.; Koelmans, W. W.; Michler, J.; Schwiedrzik, J. From 2D to 3D electrochemical microfabrication of nickel architectures at room temperature: Synthesis and characterization of microstructure and mechanical properties. *Addit. Manuf.* **2024**, *88*, 104251.
[33] Daryadel, S.; Behroozfar, A.; Morsali, S. R.; Moreno, S.; Baniasadi, M.; Bykova, J.; Bernal, R. A.; Minary-Jolandan, M. Localized pulsed electrodeposition process for three-dimensional printing of nanotwinned metallic nanostructures. *Nano Lett.* **2018**, *18*, 208–214.
[34] Funch, C. V.; Palmas, A.; Somlo, K.; Valente, E. H.; Cheng, X. W.; Poulios, K.; Villa, M.; Somers, M. A. J.; Christiansen, T. L. Targeted heat treatment of additively manufactured Ti–6Al–4V for controlled formation of Bi-lamellar microstructures. *J. Mater. Sci. Technol.* **2021**, *81*, 67–76.
[35] Liu, S. Q.; Ding, H. S.; Chen, R. R.; Guo, J. J.; Fu, H. Z. Evolution of rapidly grown cellular microstructure during heat treatment of TiAl-based intermetallic and its effect on micromechanical properties. *Intermetallics* **2021**, *132*, 107166.
[36] Zhang, J. C.; Ni, S. B.; Tang, J.; Yang, X. L. Superior electrochemical performance of NiS/Ni obtained via electrochemical corrosion. *Mater. Lett.* **2016**, *181*, 25–28.
[37] Chaabane, I.; Banerjee, D.; Touayar, O.; Cloutier, S. G. Shallow V-shape nanostructured pit arrays in germanium using aqua regia electroless chemical etching. *Materials* **2017**, *10*, 854.
[38] Yang, J. J.; Zhou, S. K.; Yang, M. T.; Zhao, S. B.; Wang, S. T.; Deng, G. L. Antireflection microstructures on a ZnS surface fabricated by femtosecond laser direct writing assisted with wet etching. *Opt. Mater.* **2025**, *159*, 116597.
[39] Xia, A. N.; He, L.; Qie, S. H.; Zhang, J. C.; Li, H. L.; He, N.; Hao, X. Q. Fabrication of an anti-icing aluminum alloy surface by combining wet etching and laser machining. *Appl. Sci.* **2022**, *12*, 2119.
[40] Xu, J.; Zhang, G. J.; Wang, L.; Wu, C. Y.; Huang, Y.; Rong, Y. M. Light nurtures plants: The picosecond laser-induced lithops-like microstructures on titanium alloy surface with broad-band ultra-low reflectivity. *Appl. Surf. Sci.* **2023**, *625*, 157199.
[41] Zhang, Y.; Liu, Q. L.; Li, J.; Yao, H. C.; Hou, Y. H.; Hou, J. Z. Large-scale fabrication of flexible antiglare film with superhydrophobic surface: Toward high transmittance and high haze. *Chem. Eng. J.* **2025**, *511*, 161805.
[42] Han, X. S.; Wang, J. B.; Wang, J. W.; Ding, L. H.; Zhang, K.; Han, J. Q.; Jiang, S. H. Micro- and nano-fibrils of manau rattan and solvent-exchange-induced high-haze transparent holocellulose nanofibril film. *Carbohyd. Polym.* **2022**, *298*, 120075.
[43] Guan, Y. H.; He, H. D.; Tang, D. X.; Guo, P. F.; Han, X. Q.; Zhang, H. X.; Xu, J. Y.; Dai, L.; Huang, Z. H.; Si, C. L. Functional cellulose paper with high transparency, high haze, and UV-blocking for perovskite solar cells. *Adv. Compos. Hybrid Mater.* **2024**, *7*, 12.
[44] Ma, Y. J.; Gou, T.; Feng, C. C.; Li, J.; Li, Y.; Huang, J. B.; Li, R. M.; Zhang, Z. Y.; Gao, X. F. Facile fabrication of biomimetic films with the microdome and tapered nanopipple hierarchical structure possessing high haze, high transmittance, anti-fouling and moisture self-cleaning functions. *Chem. Eng. J.* **2021**, *404*, 127101.
[45] Jia, C.; Li, T.; Chen, C. J.; Dai, J. Q.; Kierzewski, I. M.; Song, J. W.; Li, Y. J.; Yang, C. P.; Wang, C. W.; Hu, L. B. Scalable, anisotropic transparent paper directly from wood for light management in solar cells. *Nano Energy* **2017**, *36*, 366–373.
[46] Zhai, S. J.; Zhao, Y. H.; Zhao, H. High-efficiency omnidirectional broadband light-management coating using the hierarchical ordered-

disordered nanostructures with ultra-mechanochemical resistance. *ACS Appl. Mater. Interfaces* **2019**, *11*, 12978–12985.

[47] Sun, H.; Ji, T.; Zhou, X. Y.; Bi, H. J.; Xu, M.; Huang, Z. H.; Cai, L. P. Mechanically strong, transparent, and biodegradable wood-derived film. *Mater. Chem. Front.* **2021**, *5*, 7903–7909.

[48] Song, Y. J.; Xu, Y. L.; Li, D. Q.; Chen, S.; Xu, F. Sustainable and superhydrophobic lignocellulose-based transparent films with efficient light management and self-cleaning. *ACS Appl. Mater. Interfaces* **2021**, *13*, 49340–49347.

[49] Kim, D. H.; Dudem, B.; Jung, J. W.; Yu, J. S. Boosting light harvesting in perovskite solar cells by biomimetic inverted hemispherical architectured polymer layer with high haze factor as an antireflective layer. *ACS Appl. Mater. Interfaces* **2018**, *10*, 13113–13123.

[50] Guan, Q. F.; Ling, Z. C.; Han, Z. M.; Yang, H. B.; Yu, S. H. Ultra-strong, ultra-tough, transparent, and sustainable nanocomposite films for plastic substitute. *Matter* **2020**, *3*, 1308–1317.

[51] Wang, S. N.; Mastantuoni, G. G.; Dong, Y. Y.; Zhou, Q. Strong and transparent film of naturally aligned softwood holocellulose fibers. *Carbohyd. Polym.* **2025**, *347*, 122722.

[52] Li, S.; Cui, B. Y.; Jia, X.; Wang, W. H.; Cui, Y. T.; Ding, J. Y.; Fang, Y. Q.; Song, Y. M.; Zhang, X. Q. A cellulose-based film with self-healing performance for light management. *Ind. Crops Prod.* **2024**, *212*, 118312.

[53] Hwang, Y.; Sadhu, A.; Shin, S.; Leow, S. W.; Zhao, Z.; Deng, J. Y.; Jackman, J. A.; Kim, M.; Wong, L. H.; Cho, N. J. An intrinsically micro-/nanostructured pollen substrate with tunable optical properties for optoelectronic applications. *Adv. Mater.* **2021**, *33*, 2100566.

[54] Zhu, M. W.; Li, T.; Davis, C. S.; Yao, Y. G.; Dai, J. Q.; Wang, Y. B.; AlQatari, F.; Gilman, J. W.; Hu, L. B. Transparent and haze wood composites for highly efficient broadband light management in solar cells. *Nano Energy* **2016**, *26*, 332–339.

[55] Yao, Y. G.; Tao, J. S.; Zou, J. H.; Zhang, B. L.; Li, T.; Dai, J. Q.; Zhu, M. W.; Wang, S.; Fu, K. K.; Henderson, D. et al. Light management in plastic-paper hybrid substrate towards high-performance optoelectronics. *Energy Environ. Sci.* **2016**, *9*, 2278–2285.

[56] Zhang, C.; Zhan, Y. J.; Qiu, Y. X.; Xu, L. L.; Guan, J. G. Planar metasurface-based concentrators for solar energy harvest: From theory to engineering. *PhotoniX* **2022**, *3*, 28.

[57] Tournebize, A.; Mattana, G.; Gorisse, T.; Bousquet, A.; Wantz, G.; Hirsch, L.; Chambon, S. Crucial role of the electron transport layer and UV light on the open-circuit voltage loss in inverted organic solar cells. *ACS Appl. Mater. Interfaces* **2017**, *9*, 34131–34138.